Evaluation of Different Methods for Calculating the ROTI index over Brazilian Sector

C. S. Carmo[1], C. M. Denardini[1]; C. A. O. B. Figueiredo[1], L. C. A. Resende[1,2], D. Barros[1], G. A. S. Picanço[1], P. F. Barbosa Neto[1,3], P. A. B. Nogueira[4], J. Moro[2,5], S. S. Chen[1]

[1] National Institute for Space Research, 12227-010, S. J. dos Campos - SP, Brazil.

[2] State Key Laboratory of Space Weather, Beijing, China.

[3] Salesian University Center of São Paulo, 12600-100, Lorena - SP, Brazil.

[4] Federal Institute of Education, Science and Technology of Sao Paulo, Jacarei - SP, Brazil.

[5] Southern Regional Space Research Center – CRCRS/COCRE/INPE-MCTIC, Santa Maria-RS, Brazil.

Carolina Carmo (carolscarmo25@gmail.com)

Key Points:

- ROTI ionospheric index
- space weather
- ionospheric irregularities.

Abstract

The ROTI index based on the variation of the TEC is used to detect and characterize the ionospheric irregularities. In the present work, we present a comparative study of five different methodologies to ROTI calculation in order to evaluate the most suitable for the Brazilian region. This was performed over three GNSS stations at different latitudes: São Luís (SALU, 2°31′ S, 44°16′ W; dip: -6.60°) that is located near the dip equator; Cachoeira Paulista (CHPI, 22°40' S, 44°59' W; dip: -35.99°) which set close to the southern crest of the EIA at low latitude); and Santa Maria (SMAR, 29° 41′ S, 53° 48′ W, dip: -43.51°) a low-to-mid latitude station close to center of the SAMA region. The period of analysis covered January and December 2015. Our results show that only one out of the five techniques proposed seems to be appropriated for ROTI construction in the Brazilian sector. Our results are supported by comparison of the ROTI with TEC maps obtained over Brazil, ionograms acquired at Fortaleza (FZA0M), SALU, and CHPI ionosonde stations, and All-Sky imagers collected at the São João do Cariri, and CHPI. In addition, we were able to observe the typical irregularities of the Brazilian ionosphere by using the ROTI which we have classified as EPB.

1 Introduction

The ionospheric are kwon to interfere in the electromagnetic waves in several different ways (with a clear dependence of the wavelength) when crossed by by radio signals used in telecommunications, such as those used by the Global Navigation Satellite System (GNSS). Such effects go from enlarging the time delay caused by increases of the electron density that leads to increases in positioning errors, up to the loss-of-lock in the GNSS receiver due to the presence of Equatorial Plasma Bubbles (EPB) close to the dip equator (Farley et al., 1970; Tsunoda, 1981; Aarons et al., 1996; Pi et al., 1997; Abdu et al., 2009). The ionospheric irregularities have been widely studied in the Brazilian sector using various techniques such as ionograms from ionosonde (Abdu et al., 1982, Batista et al., 1990, Abdu et al., 2003; Abdu et al., 2012), Range-Time-Intensity (RTI) maps from VHF radars (Denardini et al., 2006, Abdu et al., 2009), images from All-Sky Imagers (ASI) observations (Pimenta et al., 2003; Paulino et al., 2011), and Total Electron Content (TEC) derived from GNSS receivers (Takahashi et al., 2014; Takahashi et al., 2015; Fagundes et al. 2016).

Among these techniques, the TEC derived from the GNSS receivers are the only ones that cover all regions of Brazil with some interpolation over few blank areas specially over the Amazon Forest. Thus, it has the potential to facilitate the observations of irregularities, allowing us to measure size and speed of propagation, among other parameters (Barros et al., 2018). Complementary (or alternatively) to the studies of the variation of the TEC derived from the GNSS, we can also study directly the fluctuations in the radio signal that are affected by the density fluctuation in the ionosphere. One of the current methodologies used to study such effects of the irregularities on GNSS signals is based on the analysis of the phase fluctuations in dual-frequency received radio signals. We can determine an index based on the time rate of different phase changes in dual-frequency signals crossing the same ionospheric volume. It is the so called the Rate Of TEC (ROT) measurement that is given in TECU/min unit (1 TECU = 10^{16} electrons/m^2) due to relationship between frequency delays caused the ionospheric volume. The ROT can describe the irregularities in different length scales (Pi et al., 1997) depending on the frequency.

The standard deviation of the ROT is used to build another index named Rate Of change of the TEC Index (ROTI), which is used for the present analysis and from which we can analyze the ionospheric irregularities more accurately (Oladipo et al., 2013). The main advantage of the ROTI over the ROT is that we simplify the problem by avoiding calculate the Differential Code Bias (DCB). Thus, once the DCB, one of the main (if not the main) factors of error, is not included in calculation, the ROTI becomes a very reliable index for estimate ionospheric variations. For instance, Pi et al. (1997) studied the geomagnetic storm occurred on 10 January 1997 based on global ROTI maps and showed that it is useful for studing the evolution of ionospheric irregularities around the globe.

In a more recent work, Liu et al. (2019b) study the plasma irregularities based on ROTI calculated with more than one constellation of satellites for the first time. They used data acquired by receivers in Asia and South America during the geomagnetic storm occurred on 16 March 2015. Their results showed that the multi-GNSS ROTI values are able to represent the temporal evolution of ionospheric irregularities during a large geomagnetic storm. Although, they found inconsistency in the magnitudes of multi-GNSS ROTIs among some GNSS receivers. Cherniak et al. (2015) also used the ROTI maps to study ionospheric irregularities in high latitudes. They found that the ROTI map represents well the development of TEC irregularities and characterizes the ionospheric responses to auroral activity in both hemispheres.

Regarding the use of ROTI in the Brazilian sector, Souza and Camargo (2019) detected ionospheric irregularities over. They used data collected at the Boa Vista (BV, 2° 49' N, 60° 40' W) station to calculate the TEC. They also showed that the ROTI index is reliable to study the temporal evolution of ionospheric irregularities over Brazil too. However, the authors took into account only one station. Thus, it was not possible to observe the propagation direction, generation, and evolution of the observed irregularities.

Therefore, once the Brazilian sector is located in a region were the magnetic equator has a large declination (~-20°) that is responsible for the EPB season to be in the South hemisphere summer and where we have the presence of the South America Magnetic Anomaly (SAMA), we decided to extend the previous study. Also, and most importantly, we have compared the five methodology to calculate the ROTI index, Pi et al. (1997), Liu et al. (2019a), Carrano et al. (2019), Cherniak et al. (2018) and Liu et al. (2019b) to define which one is the most appropriated for the Brazilian sector. After testing different techniques based on the previous works to build a reliable index capable to reproduce the effects caused by irregularities in the GNSS signals, the index was obtained from data collected by GNSS receivers operating at São Luís (SALU), Cachoeira Paulista (CHPI), and Santa Maria (SMAR) during the 17, 18, and 20 January 2015 and 25 December 2015. Finally, we compare our results with data acquired by the ionosonde installed in Fortaleza (FZA0M), SALU, and CHPI stations, as well as with images acquired by All-Sky imager installed in São João do Cariri and CHPI to validate this index.

2 Data Set

Data from GNSS, ionosondes, and All-Sky imager were collected and analyzed to obtain the ionospheric irregularities over the selected Brazilian stations SALU, CHPI and SMAR. In the following sections, we briefly describe each set of data used in this work.

2.1 GNSS Data and TEC calculation

The GNSS system allows us to determine the geospatial position with global coverage of longitude, latitude, and altitude at any point on Earth. This system is composed of GPS from the United States of America, the GLONASS of the Russian Federation, the European Union's Galileo, and Beidou from China, among others.

The data was collected by the receiver provided by the radio signal transmissions from each satellite in the constellation. It is guaranteed that at least four satellites are monitored on the Earth's surface (Monico, 2008). Also, the waves carrying the L1 and L2 bands of frequencies are transmitted by each satellite. The frequencies are generated simultaneously for users, allowing part of the effects caused by the ionosphere to be corrected.

The GPS receiver data used were obtained by the Brazilian Network of Continuum Monitoring of GNSS System (RBMC) network obtained by the Brazilian Institute of Geography and Statistics (IBGE). In addition, data were also collected from the International GNSS Service (IGS). In this work, we will use GPS receivers for the stations of SALU, CHPI and SMAR. As it is well known, the GPS satellites emit radio signals of dual-frequency f_1 and f_2 that allow determining the number of electrons along a vertical column with a section of 1 m² that goes from the satellite to the receiver. Therefore, we calculate the slant TEC (STEC), considering elevation angle higher than 30º, according to Equation 1 (Mannucci et al.,1999):

$$STEC = \frac{1}{40.3}\frac{f_1^2 \times f_2^2}{f_1^2 - f_2^2}\left[(\Phi_1 - \Phi_2) - (\lambda_1 N_1 - \lambda_2 N_2) + B_{r,s}\right], \quad (1)$$

where f_1 = 1575.42 MHz, f_2 = 1227.60 MHz, $\Phi_{1,2}$ is the phase of wave 1 and 2, $\lambda_{1,2}$ is the wavelength of 1 and 2, N is phase ambiguity, and $B_{r,s}$ is the bias of the receiver and the satellite. Thus, STEC is converted to vertical TEC (VTEC) by applying a mapping function. shown in the Equation 2:

$$VTEC = STEC\left[1 - \left(\frac{R_e \cos(\theta)}{R_e + H_{ipp}}\right)\right]^{-\frac{1}{2}}, \quad (2)$$

where R_e is the Earth radius H_{ipp} is the height of the Ionospheric Pierce Point (IPP) (in this work we consider equal to 350 km), θ is the angle of elevation in radians.
TEC is given in TEC units, in which 1 TECU equals 10^{16} electrons/m².
In this paper, we include the TEC to obtain the ROTI in the different methods as described ahead. More details about the TEC calculation are given by Takahashi et al. (2016).

2.2 Ionosonde Data

The ionosonde is an ionospheric radar that operates in variable high frequency (HF) used to investigate the ionosphere regions (Denardini et al., 2016). The data collected are echoes of the signal reflected by the ionospheric layers of corresponding electron density to the frequency of the transmitted signal. These echoes are registered in ionograms that are graphics of the transmitted frequency versus virtual height (*h'F*), which provide the electron density profile of the different regions in the ionosphere. We use ionosonde data acquired in SALU, Fortaleza (3°43' S, 38° 32' W, dip: -14.99º), and CHPI to examine the presence of irregularities observed previously in ROTI index. These ionosondes belong to the Embrace Digisonde Network and their characteristics can be found in Denardini et al. (2016). The occurrence of irregularities in the F region is shown as "Spread-F" in ionosonde data. These irregularities are aligned along the Earth's magnetic field (Spencer, 1955). Also, the Spread-F is related to the plasma bubbles, mainly during the summer (Abdu et al., 1983; Lynn et al., 2013).

2.3 All-Sky imager

The ASI is an equipment used for observations of aeroluminescence emissions in the mesosphere and ionosphere using the Hydroxyl (OH 700-900 nm), and Atomic Oxygen (OI 630 nm). Aeroluminescence operates with the two optical filters and is related to the emission of photons by the atoms and excitation of the molecules present in the Earth's atmosphere. The 630 nm image covers a horizontal extension of 1,600 km (at the zenith angle of 75°) at an altitude of 250 km, permitting the image to cover the latitudinal and longitudinal extension of the plasma depletions along the magnetic field line (Takahashi et al., 2015). Also, the ASI has a fisheye lens, with a field of view of approximately 180°, filters, lenses, CCD camera (1024 x 1024 pixels).

For the present study, we used the ASI installed in São João do Cariri (7°23' S, 36°31' W, dip: -23.35°) and CHPI. The purpose is to confirm the plasma bubbles occurrences, and therefore, to validate the ROTI index.

3 Methodology for ROTI Calculation

In this work, we use the Rate of TEC Index (ROTI), an ionospheric index used to calculated disturbances in the time variability of the ionospheric plasma. Consequently, with this index, it is possible to observe the irregularities in the plasma ionospheric well-known as plasma bubbles.

The calculation of ROTI is based on the Rate Of TEC (ROT), defined in Equation 3 (Pi et al., 1997):

$$ROT = \frac{TEC_{t_2} - TEC_{t_1}}{t_2 - t_1} = \frac{\Delta TEC}{\Delta t}, \quad (3)$$

where t is the time and $TEC_{t_{1,2}}$ is the value corresponding to the TEC at time t_1 and t_2. Notice that the ROT is based on the difference of the TEC values in two points. The ROTI was based on the standard deviation of ROT in 5 min, as in Equation 4 (Pi et al., 1997).

$$ROTI = \sqrt{< ROT^2 > - < ROT >^2}. \quad (4)$$

Where $\langle ROT \rangle$ denotes arithmetic averaging ROT during N epoch.

Therefore, the ROTI can be calculated in different forms, based on distinct methods for calculating the TEC.

In this work, we will use as reference the TEC calculation suggested by Seemala and Valladares (2011), where the absolute TEC is obtained using the satellite biases published by the University of Bern and the receiver bias is calculated minimizing the TEC variability. The software developed by this technique can automatically identify TEC depletion by analyzing the TEC trace for each satellite passage.

4 Analysis of the different techniques to ROTI calculation

We have tested five methodologies to obtain the TEC, which is necessary in the ROTI construction. Table 1 shows the list of these techniques, which shows the main characteristics of each method like rate, range values, elevations, and its reference. Notice that the sample rate is almost the same (5 minutes) in all techniques, except for the one used in Carrano et al. (2019), in which the author used a calculation that allows having a sample of 1 minute, also. Pi et al. (1997) and Carrano et al. (2019) was used the TEC data while the works of Liu et al. (2019a), Cherniak et al. (2018), Liu et al. (2019b) used the Slant TEC (STEC). The main difference between these techniques is related in the TEC calculation since some methods consider the bias while others do not consider them. A detailed description of each method is given in the next sections:
Table 1. List of the five techniques used to build the ROTI.

Method	ROT	Rate	Range values	Elevation	Reference
1	TEC	5min	0-1/0-3	>20º	Pi et al. (1997)
2	STEC	5min	0-3	-	Liu et al. (2019a)
3	TEC	1 or 5min	0-0.4	>30º	Carrano et al. (2019)
4	STEC	5min	0-8	>30º	Cherniak et al. (2018)
5	STEC	5min	0-6	>30º	Liu et al. (2019b)

Table 1. ROT, sampling rate, scale and elevation for each method used.

4.1 Method 1

The method 1 means that the TEC was calculated for consecutive times. The bias does not need to be determined since it is canceled, as shown in Equations 5 and 6 (Wanninger, 1993).

$$Rot(t_2) = \mathrm{TEC}(t_2) - TEC(t_1), \quad (5)$$

$$Rot(t_2) = S_I\big(\Phi_1(t_2) - \Phi_2(t_2) - \Phi_1(t_1) - \Phi_2(t_1)\big), \quad (6)$$

where $\Delta t = t_2 - t_1 = 1$ min, Φ = dual frequency phase, f_1 = 1575.42 MHz , f_2 = 1227.60 MHz and $S_I = \frac{1}{40.3}\frac{f_1^2 \times f_2^2}{f_1^2 - f_2^2} = 9.52 \times 10^{16} m^{-3}$. The ROTI is obtained from the ROT calculation using the Equations 3 and 4.

4.2 Method 2

The method 2 for ROTI calculation is obtained using Equation 7 and 8, and it is presented in Liu et al. (2019a).

$$ROT = \frac{STEC_{k+1} - STEC_k}{\Delta t_k}, \quad (7)$$

in which the k refers to the epoch.

Finally, the ROTI was calculated according to Equation 8.

$$ROTI = \sqrt{\frac{1}{N}\sum_{j=1}^{N}(ROT_j - ROT_{aver})^2}, \quad (8)$$

where ROT_{aver} indicates the average of the ROT.

4.3 Method 3

The method 3 is defined in Carrano et al. (2019), in which a new theory was presented for ROTI calculation. In this case, the authors considered the direct relationship of the phase structure function in the ionosphere.

The ROTI is calculated according to Equation 9.

$$ROTI^2(\delta t) = \left\langle \frac{|TEC(t + \delta t) - TEC(\delta t)|^2}{\delta t^2} \right\rangle, \quad (9)$$

where δt is the time variation. The most used sampling rates are δt = 1 and 30 s (Jacobsen, 2014).

In this method, Equation 4 is not used to calculate the ROTI.

4.4 - Method 4

Method 4 uses the STEC according to Equation 10 (Cherniak et al., 2018).

$$sTEC = \left(\frac{L_1}{f_1} - \frac{L_2}{f_2}\right)\frac{f_1^2 f_2^2}{f_1^2 - f_2^2}\frac{c}{K}, \quad (10)$$

The corresponding values of the frequencies f_1 and f_2 were presented in method 1, $L_{1,2}$ are the phase measurements corresponding to frequency 1 and 2, and the k = 40.3 m³/s².

The ROT is defined in the Equation 11.

$$ROT = \frac{sTEC_k^i - sTEC_{k-1}^i}{t_k - t_{k-1}}, \quad (11)$$

Thus, the standard deviation of the ROT in a specific time interval represents the ROTI.

4.5 Method 5

The method 5 defined by Liu et al. (2019b) uses the TEC data obtained thorough Equation 12.

$$TEC = \frac{1}{40.3}\left(\frac{f_1^2 f_2^2}{f_1^2 - f_2^2}\right)\left[(\lambda_2 L_2 - \lambda_1 L_1) - [(\lambda_2 N_2 - \lambda_1 N_1) + (d_2 - d_1)\right], \quad (12)$$

where $\lambda_{1,2}$ are the wavelengths of the frequency $f_{1,2}$, $L_{1,2}$ are the corresponding measurements of the wave, $N_{1,2}$ are the phase ambiguities corresponding to the frequencies $f_{1,2}$, and $d_{1,2}$ are the satellite and receiver bias.

The ROT is calculated according to Equation 13.

$$ROT = c \times \frac{[(\lambda_2 L_2(i) - \lambda_1 L_1(i)) - (\lambda_2 L_2(i-1) - \lambda_1 L_1(i-1))]}{(t_i - t_{i-1})}, \quad (13)$$

where c is the speed of light in a vacuum, t is the time, and i is the first position. Notice that the terms $(\lambda_2 N_2 - \lambda_1 N_1)$ and $(d_2 - d_1)$ are canceled. Therefore, after determining the TEC, it is possible to calculate the ROTI through the Equation 4.

5 Results and Discussions

In order to analyze the most appropriate method for the ROTI calculation, we use the TEC obtained by Seemala and Valladares (2011) to calculate a reliable ROTI index obtained from equation 3 and 4, that was named of method Seemala. The Method Seemala was compared to the ROTI estimation by using the methods 1 to 5 calculated from the relative TEC described in the methodology section. The main aim is to obtain the most appropriate method for the ROTI index calculation in Brazilian sector. The comparison was obtained by studying the correlation coefficient and by the linear fit.

Figure 1 shows the ROTI calculation for an equatorial station, São Luís on December 25, 2015. It was obtained by using the TEC obtained by Seemala and Valladares (2011), where we call Method Seemala.

Figure 1 shows the daily variation of ROTI, where it is possible to notice considerable ROTI values between 0-4 UT (UT stands for Universal Time and LT stands for Local Time, UT=LT+3h) and 22- 24 UT, that is, at night. For times throughout the day, ROTI remained low, with values below 1 TECU/min. It can indicate that short time TEC oscillations are observed at night time only, which may be a strong indication of plasma irregularities. With this chart, we intend to compare it with the other methods. Based on the most appropriate method to be used, we will carry out a study to assess which phenomenon caused this increase in ROTI at night.

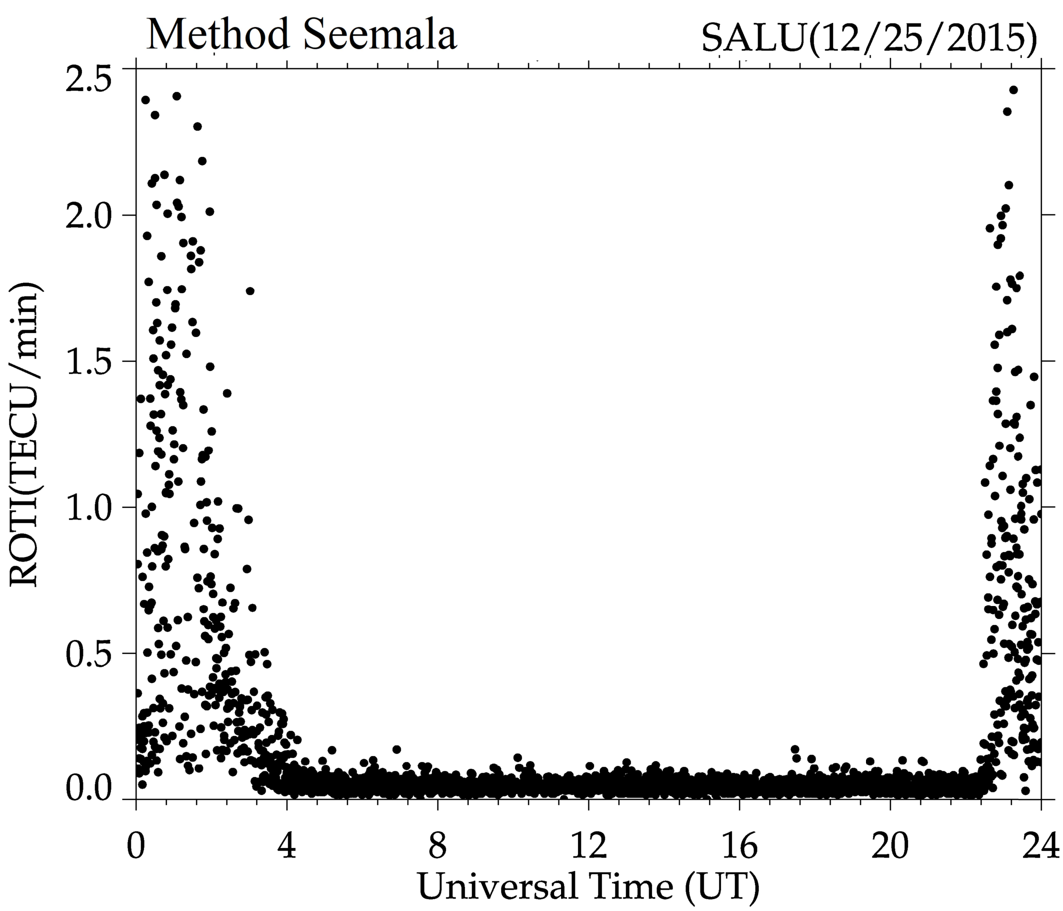

Figure 1. ROTI index obtained with the TEC calculated by the Seemala program (Seemala; Valladares, 2011), for São Luis, on December 25, 2015.

Therefore, all the results of the methods used in this work (1-5) are compared with the results presented in Figure 1.

Figure 2 shows the time variation of ROTI for São Luis on December 25, 2015 by using five (5) methods described in the methodology section. The relative TEC was calculated by using the Receiver Independent Exchange Format (RINEX) file, finally we compare with Figure 1.

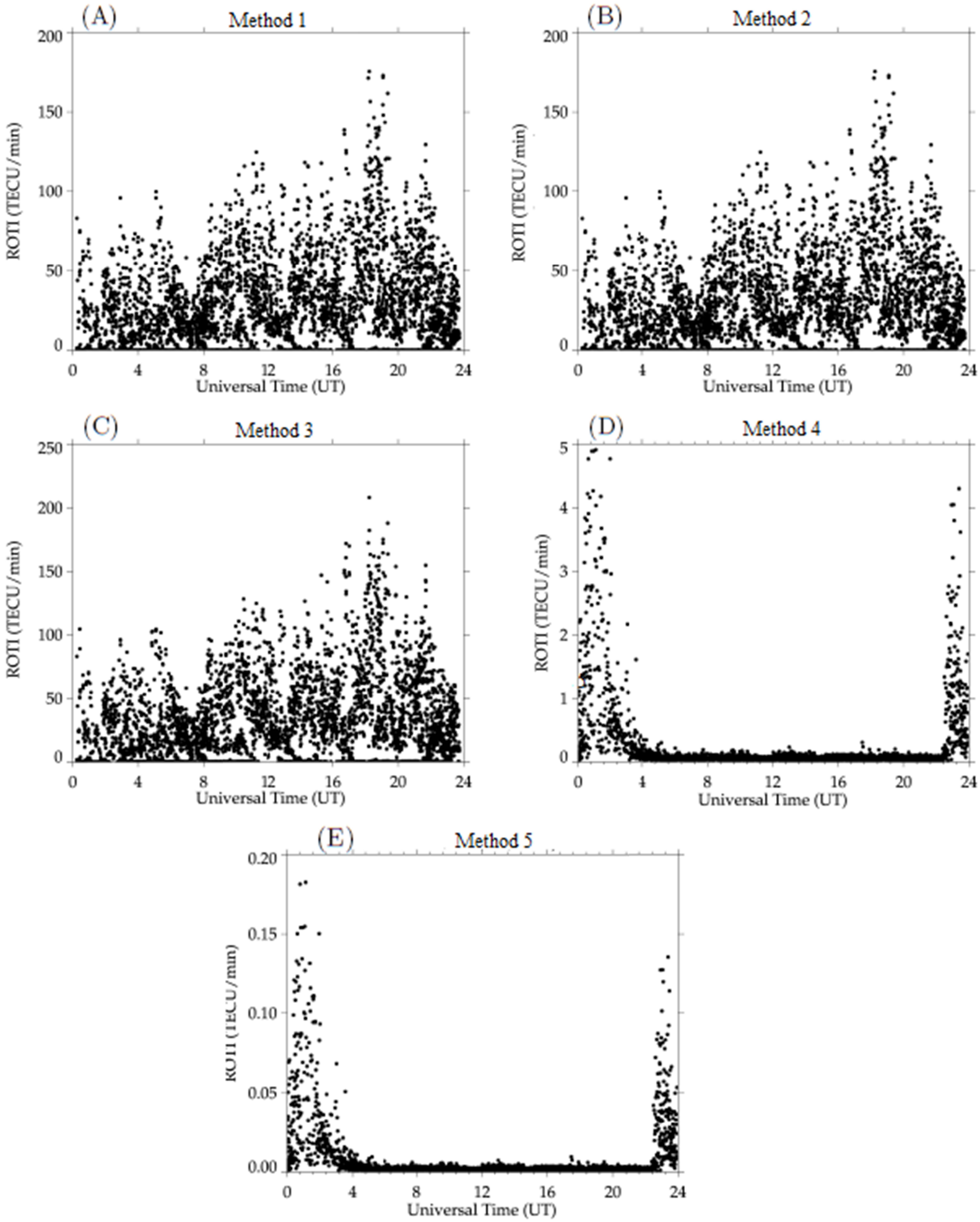

Figure 2. ROTI index calculated due to the calculation of the relative TEC, where (a) method 1, (b) method 2, (c) method 3, (d) method 4 and (e) method 5, for SALU on 25 December 2015.

It is possible to observe in Figure 2 that the results of methods 4 and 5 (letters d and e) shows high variabilities from 0 to 4 UT and from 23 to 24 UT, which is a clear evidence of TEC disturbances associated to nighttime plasma irregularities. The methods 4 and 5 show similarities to the ones observed in Figure 1. On the other side, the methods 1, 2, and 3 do show TEC oscillations for the whole day (from 0 to 24 UT), the temporal variation is significantly different from the method Seemala.

In the Figure 3 we present the ROTI values by using the method Seemala as function of the different Metlhod calculated by the Relative TEC. The Linear Fit is shown together with the corresponding correlation coefficient. We may note that values of the correlation coefficient (R) for linear fits was R = 0.08, 0.08, 0.07, 0.88, 0.84 for methods 1, 2, 3, 4 and 5, respectively. The methods 1, 2 and 3 shows no correlation to method Seemala, methods 4 shows very strong correlation and Method 5 have a moderate correlation. A summary with the coefficient correlation is given in Table 2.

By analyzing the Linear and Angular coefficient we can see method 1, 2 and 3 present a very small angular coefficient, been an almost flat curve and no linear dependence. On the other side, Method 4 (Method 5) present almost zero value for linear coefficient and 0.5 (~17.4) for angular coefficient.

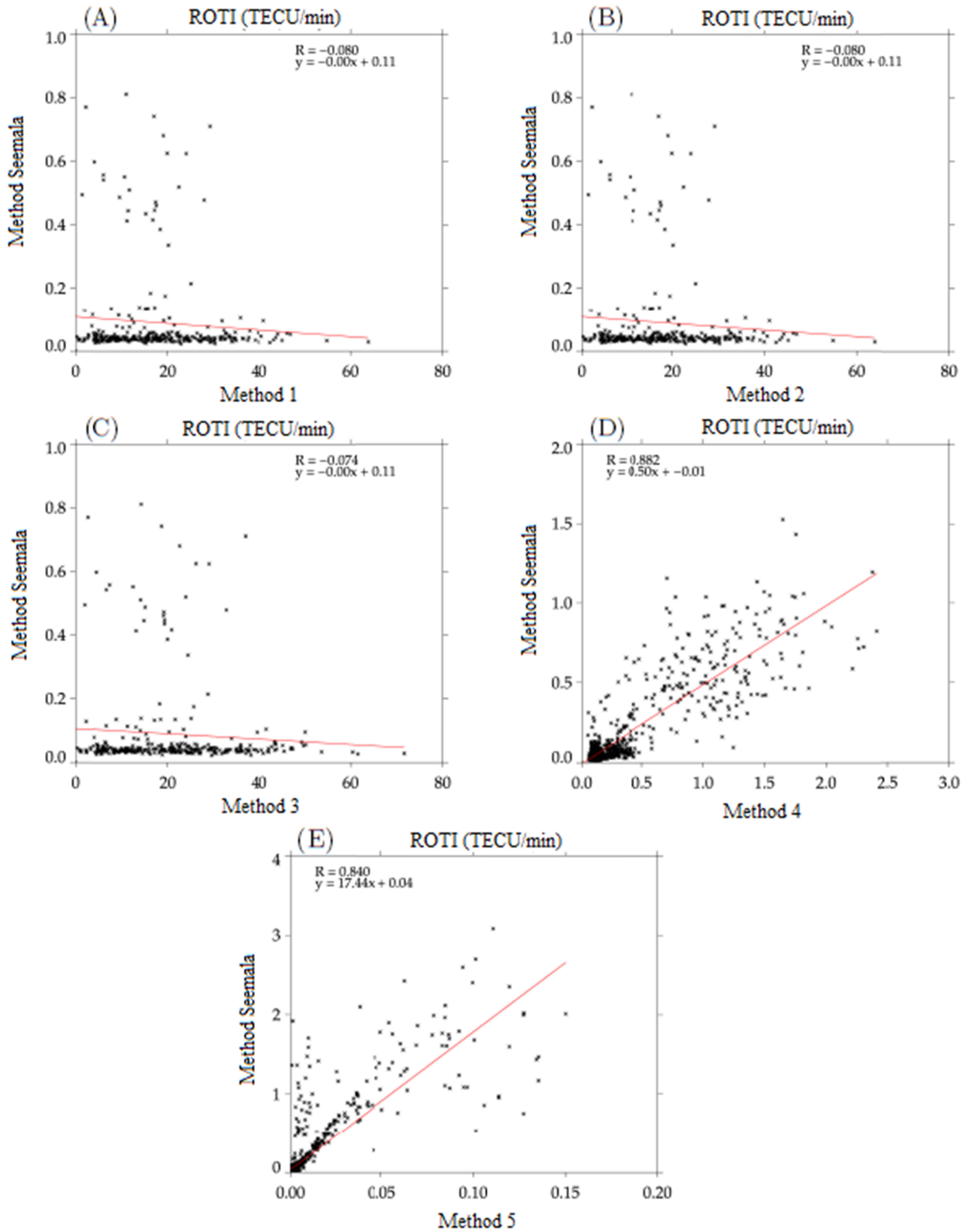

Figure 3. Correlation between method 1 using Seemala and relative TEC using (a) method 1, (b) method 2, (c) method 3, (d) method 4 and (e) method 5.

The coefficient correlation is given in Table 2.

Figure	Method	Correlation
a	1	0.08
b	2	0.08
c	3	0.07
d	4	0.88
e	5	0.84

Table 2. The coefficient correlation for each method used.

With methods 1, 2, 3 it is possible to perceive the need to use the bias, so when compared to the ROTI calculated with the Seemala program, this discrepancy in the curve is perceived and consequently does not present a good correlation. On the other hand, methods 4 and 5 do not require the calculation of the bias, showing a better correlation when compared to Seemala, however, method 4 still proved to be more efficient, presenting the best results among the 5 methods. Notice that the method in Figure 3d has a best correlation of 0.88. Therefore, to calculate the ROTI index, the method 4 is the most suitable over low latitudes.

For the case studies presented in this article we uses the method 4.

5.1 Applying the Method 4

Considering method 4 the most appropriated to ROTI calculation, we used 3 stations, SALU, CHPI, and SMAR for a deeper study of the ionospheric irregularities. In Figure 4 shows the time variation of ROTI on December 25, for SALU (top panel on the left), CHPI (top panel on the right) and SMAR (bottom panel). We can see ROTI reaches values up to 5 TECU/min in nighttime (0-4 UT and 23-24 UT), however it is not observed behavior over CHPI and SMAR (ROTI < 1 TECU/min).

Pi et al. (1997) considered ROTI values greater than 2 TECU/min could be associated to ionospheric irregularities. Since our oscillation reaches 5TECU/min at night time at an equatorial station, but no significant discrepancies was observed on the low latitudes stations, we have used a multiintrumental analysis in order to identify if it may be considered a plasma bubble event.

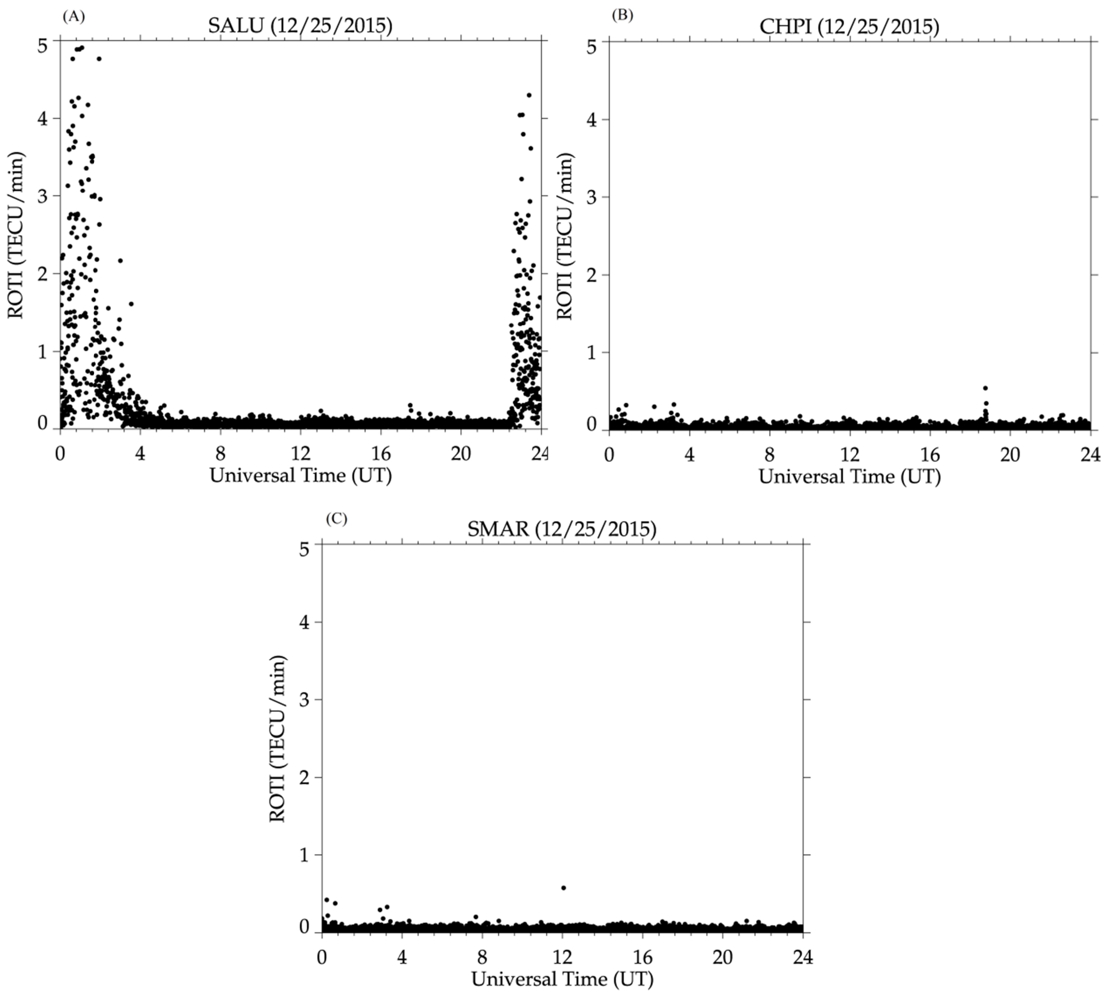

Figure 4. ROTI index for SALU (a), CHPI (b) and SMAR (c) stations, for December 25, 2015.

To confirm whether the increase in the ROTI index observed on the figure 4 is related to plasma bubbles, we present in Figure 5 the TEC map at the same night (23:40 UT on December 25, 2015) over the South America region on the left (Panel a) and we plot the ionograms at the same time on the right for SALU (Panel b) and CHPI (Panel c). We have no ionogram data for SMAR station, as well as no measurements of All-Sky imager the three stations in this night.

By analyzing the ionogram of SALU, we can observe the presence of Spread-F, with do indicates a plasma irregularity over this equatorial station, in agreement to the high values of ROTI at same station. However, no Spread F was observed at low latitude (CHPI), which is also in agreement to the no observation of oscillation on the ROTI index at same station. It may indicate that the plasma irregularities developed over the equator do not reach the low latitude CHPI station. The TEC map at the left side of Figure 5 present the well know post sunset Equatorial Ionization Anomaly. Some irregular TEC distribution can be seen on the Southern crest at around (10ºS; 40ºW) and (12ºS; 45º W), it do characterizes TEC depletion running through these longitudes that is a clear signature of a plasma bubble penetrating into the southern crest of EIA. The TEC map clearly shows the presence of the plasma bubble evolution, however it has not arrived over CHPI location been the reason for not seen the Spread-F over the ionogram.

Even though there are no data available from imagers and ionosonde in SMAR, it is possible to make the analysis only with the TEC map, and it can be confirmed that the high ROTI values were due to a plasma irregularity associated to a plasma bubble event.

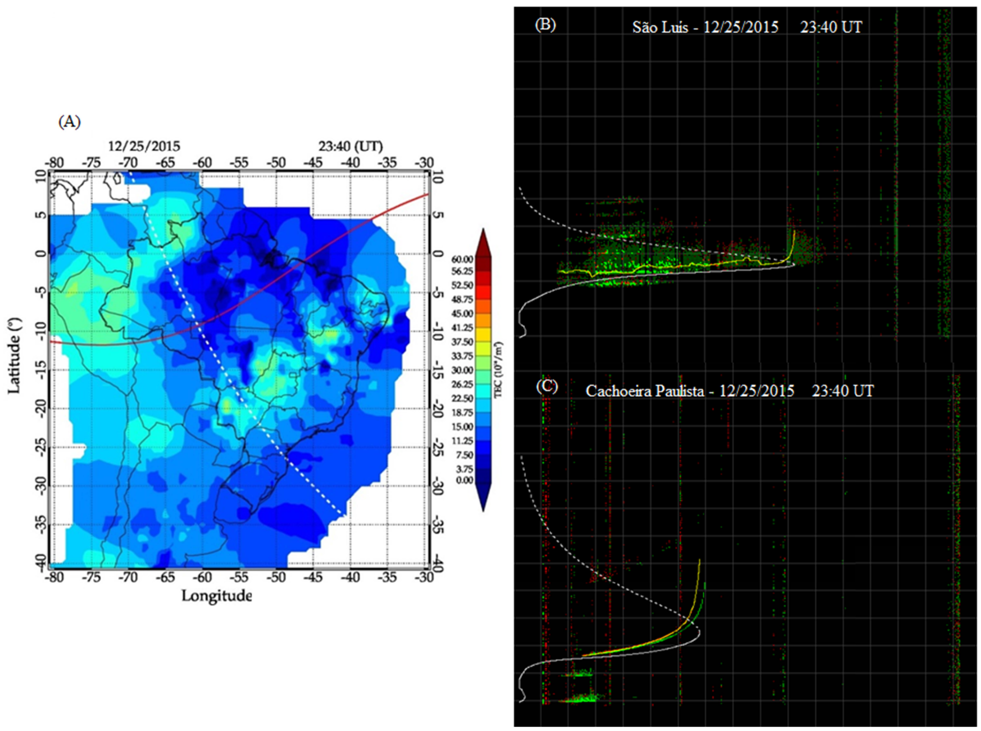

Figure 5. (a) Map of TEC, (b) Ionogram in SALU and (c) Ionogram in CHPI, on December 25, 2015, at 11:40 pm UT.

Additionally, we performed the same analysis in January 17, 18, and 20, 2015. Figure 7 shows the ROTI index for the SALU, CHPI, and SMAR stations. In the three regions we observe increases in night hours. In SALU, the index reaches 3 TECU/min around 0-4 UT and 23-24UT. In CHPI, ROTI values greater than 3 TECU/min between 0-4UT and 23-24UT. In Santa Maria, ROTI values greater than 1 TECU/min is around 0-4 UT only.

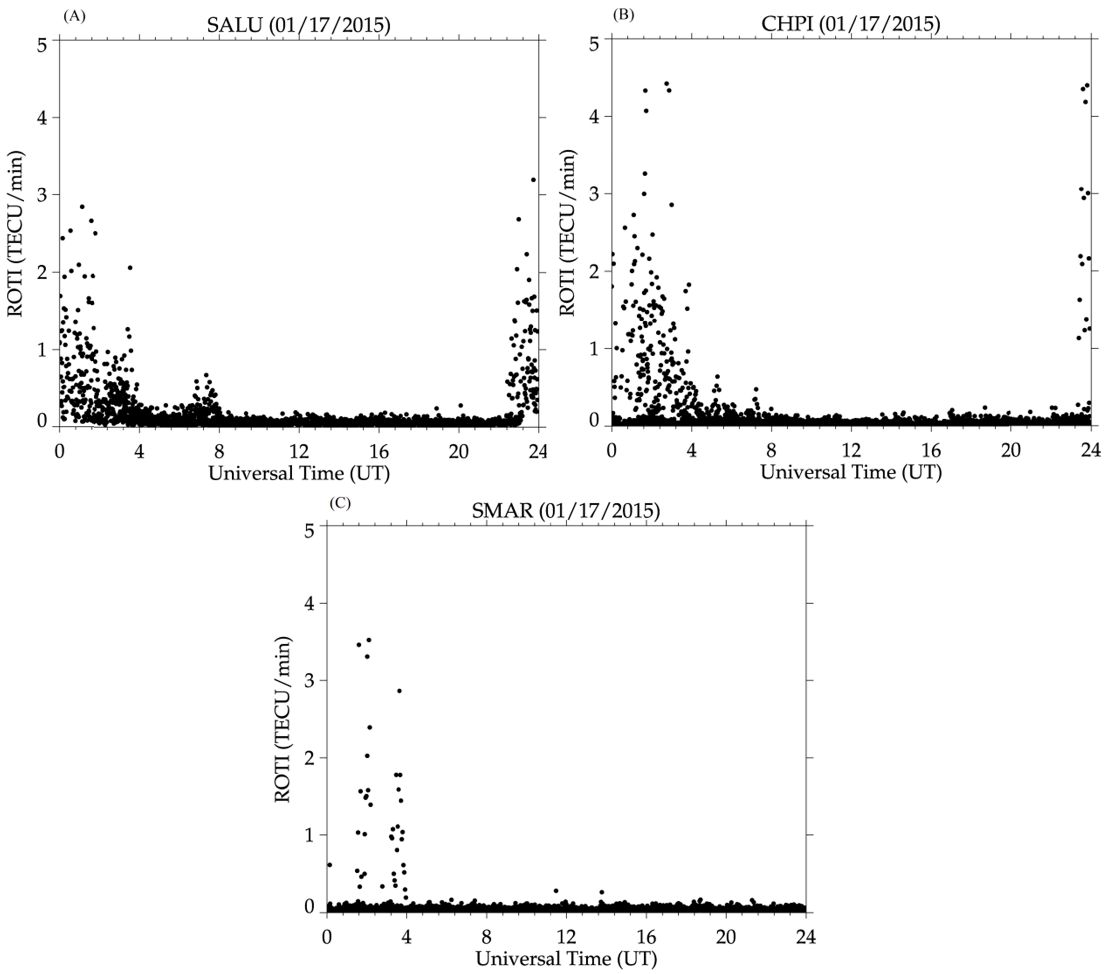

Figure 6. ROTI index for SALU (a), CHPI (b) and SMAR (c) stations, for January 17, 2015.

By using ionograms at low latitudes station (Fortaleza e CHPI), Figure 7, we have observed the presence of spread F, in same time that high values of ROTI was observed. We do have observed that the values of ROTI at CHPI are higher than compared with the others stations. Such observation is in agreement to the observation of Seba et al., (2018) in the West Africa.

Figure 7 shows the South America TEC Map (panel a), All-sky imager in São João do Cariri (panel b) and CHPI (panel c), and the ionograms over Fortaleza (Panel d) and CHPI (Panel e) station in the January, 17, 2015. Indeed, from the TEC MAP we do can see a strong TEC depletion over the Southern Crest of the EIA extending at least over -25ºS, which seem to be a field aligned irregularities. By simultaneous observation we have the All-Sky images over Sao Joao do Cariri and CHPI for where a strong plasma bubble may be identified in both station, such observation is a clear evidence of the passage of the irregularities all around the longitudes.

Such TEC depletion, the presence of the plasma bubble in the All-Sky images and the Spread-F occurrence in the ionograms corroborates to prove that the ROTI index adopted in present manuscript has potential to work as an alert to the presence of plasma bubble. ROTI index has also the advantage to be a local index to indicate the presence of plasma irregularities that affect large ionospheric error range for single-frequency positioning system. Indeed, it may be a potential parameter for the purpose of space weather application.

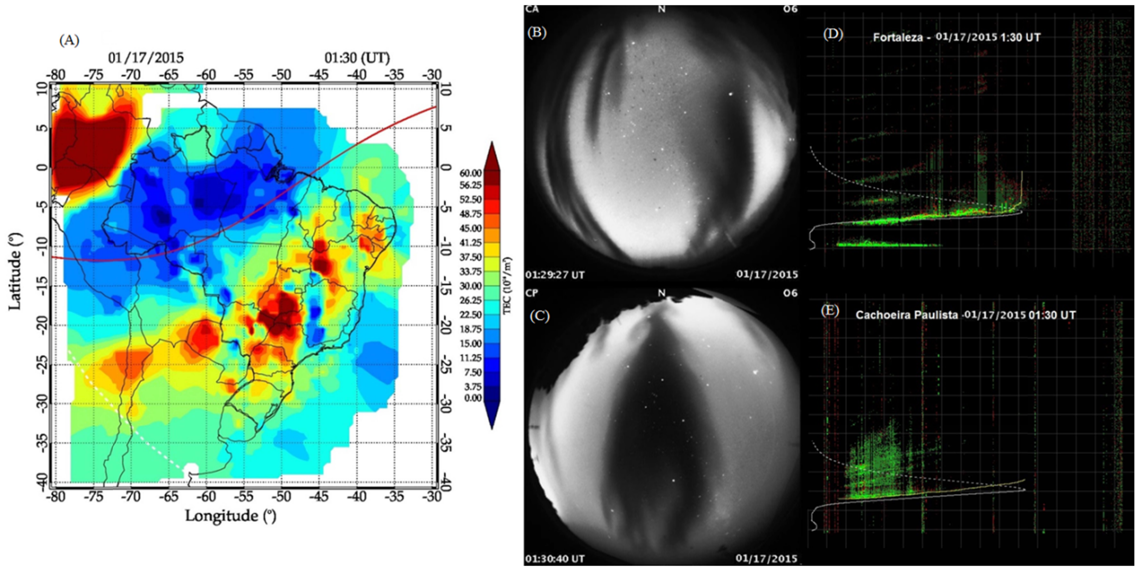

Figure 7. (a) Map of TEC, All sky imager in (b) São João do Cariri and (c) CHPI, the ionograms of the (d) Fortaleza and (e) CHPI station, on January 17, 2015, at 1:30 UT.

We can see the plasma bubbles in the TEC map, in the imagers in São João do Cariri and in CHPI, and the appearance of Spread-F in Fortaleza and CHPI in the ionograms. With that, we can confirm that for SALU and CHPI there was a plasma bubble on that day, which showed an increase in the ROTI graph. Additionally, we can see that even if there is no equipment available in SMAR, ROTI can confirm the appearance of a plasma bubble.

The same analysis made for the 17th of January was also made for the 18th and 20th of January 2015, and we obtained similar results.

With the TEC Map, All-Sky imagers and ionosonde, it was possible to confirm what was shown in the ROTI graphs, that the 17th, 18th and 20th of January obtained plasma bubbles, and these reached not only the equatorial region but also mid-latitudes, which can be observed in SMAR.

6 Conclusions

We have studied the ionospheric plasma irregularities by using the ROTI index to identify the presence of plasma bubble over the equatorial and low latitudes stations of Brazilian region, we have compared five different approach for ROTI calculations. In order to find the best method for ROTI in Brazilian sector we have compared each method to the Seemala; Valladares 2011. Our main findings are summarized below.

1. The methodology of Cherniak et al., 2018 have presented the highest correlation to method Seemala.
2. By using Cherniak et al., 2018 methodology to ROTI calculation all irregularities larger than 1 TECU/min has occurred at nighttime.

3. Methods 1, 2 and 3 have presented high values of ROTI during the whole day, the TEC disturbances in daytime need further investigation since it cannot be associated to the presence of plasma bubble.
4. We have compared the Method 4 ROTI irregularities observed to observations of Digisondes, All-Sky Images and TEC Map. In all cases analyzed, the presence of plasma bubble has been observed in different instruments since the ROTI index has reached values greater than 1 TECU/min.
5. With the case study, done for the 17th, 18th and 20th of January 2015, higher ROTI values were observed in low latitude station (CHPI), which was caused by the crest of the EIA.

Finally, we can conclude, that the technique used can be used for any study, being able to match reliability even when there is no measurement equipment in the studied regions.

Acknowledgments, Samples, and Data

The authors thank the Embrace/INPE Space Weather Program for providing the TEC maps, ionograms and images by All-Sky imager (http://www.inpe.br/spaceweather), the IBGE for providing the satellite data (Rinex) (https://www.ibge.gov.br/geociencias/downloads-geociencias.html) and the program with calculate the TEC (https://seemala.blogspot.com/). C. S. Carmo thanks Capes/MEC (Grant 88882.330725/2019-01). C. M. Denardini thanks CNPq/MCTIC (Grant 303643/2017-0). C. A. O. B., Figueiredo thanks FAPESP (Grant 2018/09066-8). L. C. A. Resende thanks the China-Brazil Joint Laboratory for Space Weather (CBJLSW), National Space Science Center (NSSC), Chinese Academy of Sciences (CAS) for supporting her Postdoctoral fellowship. D. Barros thanks CNPq/MCTIC (Grant 300974/2020-5). G. A. S. Picanço thanks Capes/MEC (Grant 88887.351778/2019-00). P. F. Barbosa Neto thanks Capes/MEC (Grant 1622967). J. Moro thanks the China-Brazil Joint Laboratory for Space Weather (CBJLSW), National Space Science Center (NSSC), Chinese Academy of Sciences (CAS) for supporting his Postdoctoral fellowship, and the CNPq/MCTIC (Grant 429517/2018-01). S. S. Chen thanks Capes/MEC (Grant 88887.362982/2019-00).

References

Aarons, J., Mendillo, M., Yantosca, R., & Kudeki, E. (1996). GPS phase fluctuations in the equatorial region during the MISETA 1994 campaign. *Journal of Geophysical Research*: *Space Physics*, 101(A12), 26851-26862. DOI: https://doi.org/10.1029/96JA00981.

Abdu, M. A., Batista, I. S., Reinisch, B. W., MacDougall, J. W., Kherani, E. A., & Sobral, J. H. A. (2012). Equatorial range spread F echoes from coherent backscatter, and irregularity growth processes, from conjugate point digital ionograms. *Radio Science*, 47(06), 1-8. DOI: 10.1029/2012RS005002

Abdu, M. A., Batista, I. S., Takahashi, H., MacDougall, J., Sobral, J. H., Medeiros, A. F., & Trivedi, N. B. (2003). Magnetospheric disturbance induced equatorial plasma bubble development and dynamics: A case study in Brazilian sector. *Journal of Geophysical Research: Space Physics*, 108(A12).

Abdu, M. A., Kherani, E. A., Batista, I. S., De Paula, E. R., Fritts, D. C., & Sobral, J. H. A. (2009). Gravity wave initiation of equatorial spread F/plasma bubble irregularities based on observational data from the SpreadFEx campaign. *Ann. Geophys*, 27(7), 2607-2622. DOI: https://doi.org/10.1029/2002JA009721.

Abdu, M. A., De Medeiros, R. T., Sobral, J. H. A., & Bittencourt, J. A. (1983). Spread F plasma bubble vertical rise velocities determined from spaced ionosonde observations. *Journal of Geophysical Research: Space Physics*, 88(A11), 9197-9204. DOI: https://doi.org/10.1029/JA088iA11p09197.

Abdu, M. A., De Medeiros, R. T., & Sobral, J. H. A. (1982). Equatorial spread F instability conditions as determined from ionograms. *Geophysical Research Letters*, *9*(6), 692-695. DOI: https://doi.org/10.1029/GL009i006p00692.

Adewale, A. O., Oyeyemi, E. O., Adeniyi, J. O., Adeloye, A. B., & Oladipo, O. A. (2011). Comparison of total electron content predicted using the IRI-2007 model with GPS observations over Lagos, Nigeria. 94.20. dt; 94.20. Cf.

Barros, D., Takahashi, H., Wrasse, C. M., & Figueiredo, C. A. O. (2018). Characteristics of equatorial plasma bubbles observed by TEC map based on ground- based GNSS receivers over South America. In *Annales Geophysicae* (Vol. 36, No. 1, pp. 91-100). Copernicus GmbH. DOI: https://doi.org/10.5194/angeo-36-91-2018.

Batista, I. S., Abdu, M. A., & Medrano, R. A. (1990, May). Magnetic activity effects on range type spread-F and vertical plasma drifts at Fortaleza and Huancayo as studied through ionosonde measurements and theoretical modelling. In *Annales Geophysicae* (Vol. 8, pp. 357-364).

Booker, H. G. A local reduction of f-region ionization due to missile transit. *Journal of Geophysical Research*, Wiley Online Library, v. 66, n. 4, p. 1073–1079, 1961. DOI: https://doi.org/10.1029/JZ066i004p01073.

Calvert, W.; Cohen, R. The interpretation and synthesis of certain spread-f configurations appearing on equatorial ionograms. *Journal of Geophysical Research*, Wiley Online Library, v. 66, n. 10, p. 3125–3140, 1961. DOI: https://doi.org/10.1029/JZ066i010p03125.

Carrano, C. S., Groves, K. M., & Rino, C. L. (2019). On the Relationship Between the Rate of Change of Total Electron Content Index (ROTI), Irregularity Strength (CkL), and the Scintillation Index (S4). *Journal of Geophysical Research: Space Physics*, 124(3), 2099-2112. DOI: https://doi.org/10.1029/2018JA026353.

Cherniak, I., Krankowski, A., & Zakharenkova, I. (2018). ROTI Maps: a new IGS ionospheric product characterizing the ionospheric irregularities occurrence. *GPS Solutions*, 22(3). DOI: https://doi.org/10.1007/s10291-018-0730-1.

Cherniak, I., Zakharenkova, I., & Redmon, R. J. (2015). Dynamics of the high-latitude ionospheric irregularities during the 17 March 2015St. Patrick's Day storm: Ground-based GPS measurements. *Space Weather*, 13(9), 585-597. DOI: 10.1002/2015SW001237.

Denardini, C. M., Abdu, M. A., De Paula, E. R., Wrasse, C. M., & Sobral, J. H. A. (2006). VHF radar observations of the dip equatorial E-region during sunset in the Brazilian sector. DOI: 10.5194/angeo-24-1617-2006.

Denardini, C. M., Dasso, S., & Gonzalez-Esparza, J. A. (2016). Review on space weather in Latin America. 3. Development of space weather forecasting centers. *Advances in Space Research*, 58(10), 1960-1967. DOI: https://doi.org/10.1016/j.asr.2016.03.011.

de Jesus, R., Batista, IS, Takahashi, H., de Paula, ER, Barros, D., Figueiredo, CAOB, et al. (2019). Morphological features of ionospheric scintillations during high solar activity using GPS observations over the South American sector. *Journal of Geophysical Research: Space Physics*.. DOI: https://doi.org/10.1029/2019JA027441.

Fagundes, P. R., Cardoso, F. A., Fejer, B. G., Venkatesh, K., Ribeiro, B. A. G., & Pillat, V. G. (2016). Positive and negative GPS-TEC ionospheric storm effects during the extreme space weather event of March 2015 over the Brazilian sector. *Journal of Geophysical Research: Space Physics*, 121(6), 5613–5625. https://doi.org/10.1002/2015JA022214.

Farley, D. T., Balsey, B. B., Woodman, R. F., & McClure, J. P. (1970). Equatorial spread F: Implications of VHF radar observations. *Journal of Geophysical Research*, 75(34), 7199-7216. DOI: https://doi.org/10.1029/JA075i034p07199.

Jacobsen, K. S. (2014). The impact of different sampling rates and calculation time intervals on ROTI values. *Journal of Space Weather and Space Climate*, 4, A33. DOI: https://doi.org/10.1051/swsc/2014031

Kelley, M. C., Fejer, B. G., & Gonzales, C. A. (1979). An explanation for anomalous equatorial ionospheric electric fields associated with a northward turning of the interplanetary magnetic field. *Geophysical Research Letters*, 6(4), 301-304. DOI: https://doi.org/10.1029/GL006i004p00301.

Liu, Z., Yang, Z., Xu, D., & Morton, Y. J. (2019). On inconsistent ROTI derived from multiconstellation GNSS measurements of globally distributed GNSS receivers for ionospheric irregularities characterization. *Radio Science*, 54(3), 215-232. DOI: 10.1029/2018RS006596.

LIU, Yang, et al. Analyzing Ionosphere TEC and ROTI Responses on 2010 August High Speed Solar Winds. IEEE Access, 2019, 7: 29788-29804. DOI: DOI: 10.1109/ACCESS.2019.2897793.

Lynn, K. J. W., Otsuka, Y., & Shiokawa, K. (2013). Ionogram-based range-time displays for observing relationships between ionosonde satellite traces, spread F and drifting optical plasma depletions. *Journal of Atmospheric and Solar-Terrestrial Physics*, 98, 105-112. DOI: https://doi.org/10.1016/j.jastp.2013.03.020.

Mannucci, A. J., B. A. Iijima, U. J. Lindqwister, X. Pi, L. Sparks, and B. D. Wilson (1999), GPS and ionosphere, in Review of *Radio Science* 1996–1999, edited by W. R. Stone, pp. 625–665, Int. Union of Radio Sci, Ghent, Belgium.

Okoh, D., Rabiu, B., Shiokawa, K., Otsuka, Y., Segun, B., Falayi, E., ... & Kaka, R. (2017). First Study on the Occurrence Frequency of Equatorial Plasma Bubbles over West Africa Using an All-Sky Airglow Imager and GNSS Receivers. *Journal of Geophysical Research: Space Physics*, 122(12), 12-430. DOI: https://doi.org/10.1002/2017JA024602.

Oladipo, O. A., & Schüler, T. (2013). Equatorial ionospheric irregularities using GPS TEC derived index. *Journal of atmospheric and solar-terrestrial physics*, 92, 78-82. DOI: https://doi.org/10.1016/j.jastp.2012.09.019.

Paulino, I., Medeiros, A. F. D., Buriti, R. A., Takahashi, H., Sobral, J. H. A., & Gobbi, D. (2011). Plasma bubble zonal drift characteristics observed by airglow images over Brazilian tropical region. *Revista Brasileira de Geofísica*, 29(2), 239-246. DOI: https://doi.org/10.1590/S0102-261X2011000200003.

Pi, X., Mannucci, A. J., Lindqwister, U. J., & Ho, C. M. (1997). Monitoring of global ionospheric irregularities using the Worldwide GPS Network. *Geophysical Research Letters*, 24(18), 2283–2286. https://doi.org/10.1029/97GL02273.

Pimenta, A. A., Bittencourt, J. A., Fagundes, P. R., Sahai, Y., Buriti, R. A., Takahashi, H., & Taylor, M. J. (2003). Ionospheric plasma bubble zonal drifts over the tropical region: a study using OI 630nm emission all-sky images. *Journal of Atmospheric and Solar-Terrestrial Physics*, 65(10), 1117-1126. DOI: https://doi.org/10.1016/S1364-6826(03)00149-4.

Pitteway, M.; Cohen, R. A waveguide interpretation of temperate-latitude spread f on equatorial ionograms. *Journal of Geophysical Research*, Wiley Online Library, v. 66, n. 10, p. 3141–3156, 1961 DOI: https://doi.org/10.1029/JZ066i010p03141.

Rao, P. R., Krishna, S. G., Niranjan, K., & Prasad, D. S. V. V. D. (2006). Temporal and spatial variations in TEC using simultaneous measurements from the Indian GPS network of receivers during the low solar activity period of 2004/ 2005.

Rishbeth 1971 H Rishbeth. Polarization fields produced by winds in the equatorial F region. *Planetary and Space Science*, 19 (1971), pp. 357-369 DOI: https://doi.org/10.1016/0032-0633(71)90098-5.

Sarudin, I., Hamid, N. S. A., Abdullah, M., & Buhari, S. M. (2017, May). Investigation of zonal velocity of equatorial plasma bubbles (EPBs) by using GPS data. *In Journal of Physics: Conference Series* (Vol. 852, No. 1, p. 012014). IOP Publishing. DOI: http://dx.doi.org/10.1088/1742-6596/852/1/012014.

Seba, E. B., Nigussie, M., & Moldwin, M. B. (2018). The relationship between equatorial ionization anomaly and nighttime equatorial spread F in East Africa. *Advances in Space Research*, 62(7), 1737-1752. DOI: https://doi.org/10.1016/j.asr.2018.06.029.

Seemala, G. K., & Valladares, C. E. (2011). Statistics of total electron content depletions observed over the South American continent for the year 2008. *Radio Science*, 46(5). DOI: https://doi.org/10.1029/2011RS004722.

Souza, A. L. C. D., & Camargo, P. D. O. (2019). Comparison of gnss indices, ionosondes and all-sky imagers in monitoring the ionosphere in brazil during quiet and disturbed days. *Boletim de Ciências Geodésicas*, 25(SPE). DOI: https://doi.org/10.1590/s1982-21702019000s00005.

Spencer, M. The shape of irregularities in the upper ionosphere. *Proceedings of the Physical Society*. Section B, IOP Publishing, v. 68, n. 8, p. 493, 1955.

Takahashi, H., Costa, S., Otsuka, Y., Shiokawa, K., Monico, J. F. G., Paula, E., ... & Ivo, A. S. (2014). Diagnostics of equatorial and low latitude ionosphere by TEC mapping over Brazil. *Advances in Space Research*, 54(3), 385-394. DOI: https://doi.org/10.1016/j.asr.2014.01.032.

Takahashi, H., Wrasse, C. M., Otsuka, Y., Ivo, A., Gomes, V., Paulino, I., ... & Shiokawa, K. (2015). Plasma bubble monitoring by TEC map and 630 nm airglow image. *Journal of Atmospheric and Solar-Terrestrial Physics*, 130, 151-158. DOI: https://doi.org/10.1016/j.jastp.2015.06.003.

Tsunoda, R. T. (1981). Time evolution and dynamics of equatorial backscatter plumes 1. Growth phase. *Journal of Geophysical Research*: Space Physics, 86(A1), 139-149. DOI: https://doi.org/10.1029/JA086iA01p00139.

Valladares, C.; Villalobos, J.; Hei, M.; Sheehan, R.; Basu, S.; Mackenzie, E.; Doherty, P.; Rios, V. Simultaneous observation of traveling ionospheric disturbances in the northern and southern hemispheres. *Ann. Geophys*, v. 27, p. 1501–1508, 2009. DOI: 10.5194/angeo-27-1501-2009.

Wanninger, L. (1993). The occurrence of ionospheric disturbances above Japan and their effects on precise GPS positioning. *Proceedings of the CRCM*, 93, 6-11.